Advances in Applied Mathematics and Mechanics
Adv. Appl. Math. Mech., Vol. **14**, No. x, pp. 1-29

DOI: 10.4208/aamm.OA-2021-0126
xxx 2022

Image Segmentation via Fischer-Burmeister Total Variation and Thresholding

Tingting Wu[1], Yichen Zhao[1], Zhihui Mao[1], Li Shi[1], Zhi Li[2,*] and Yonghua Zeng[3,*]

[1] *School of Science, Nanjing University of Posts and Telecommunications, Nanjing, Jiangsu 210023, China*
[2] *The Department of Computer Science and Technology, Shanghai Key Laboratory of Multidimensional Information Processing, East China Normal University, Shanghai 200241, China*
[3] *College of Field Engineering, PLA Army Engineering University, Nanjing, Jianhsu 210007, China*

Received 20 April 2021; Accepted (in revised version) 16 July 2021

Abstract. Image segmentation is a significant problem in image processing. In this paper, we propose a new two-stage scheme for segmentation based on the Fischer-Burmeister total variation (FBTV). The first stage of our method is to calculate a smooth solution from the FBTV Mumford-Shah model. Furthermore, we design a new difference of convex algorithm (DCA) with the semi-proximal alternating direction method of multipliers (sPADMM) iteration. In the second stage, we make use of the smooth solution and the K-means method to obtain the segmentation result. To simulate images more accurately, a useful operator is introduced, which enables the proposed model to segment not only the noisy or blurry images but the images with missing pixels well. Experiments demonstrate the proposed method produces more preferable results comparing with some state-of-the-art methods, especially on the images with missing pixels.

AMS subject classifications: 65K10, 68U10, 94A08

Key words: Image segmentation, Fischer-Burmeister total variation, difference of convex algorithm, sPADMM, K-means method.

1 Introduction

Image segmentation is to divide an image into distinct objects in reality. In recent years, many great approaches have been proposed to handle this problem [1–7]. In [8], an en-

*Corresponding author.
Emails: zli@cs.ecnu.edu.cn (Z. Li), protege_user@126.com (Y. Zeng)

ergy minimization approach was proposed by Mumford and Shah named Mumford-Shah model, and their idea is to find a suitable piecewise continuous or constant solution u for a given image f. The Mumford-Shah model has been widely used in various aspects [9–13]. Moreover, its variants have been extensively used in image processing owing to their flexibility and adaptation in numerical implementation. Denote $\Omega\subset\mathbb{R}^2$ as a bounded and continuous open set, $f:\Omega\to\mathbb{R}$ as a given grayscale image. In general, we set $f\in[0,1]$, therefore $f\in L^\infty(\Omega)$. Especially, the energy minimization problem for image segmentation is as follows

$$E(u,\Gamma)=\mathcal{H}^1(\Gamma)+\frac{\mu}{2}\int_{\Omega\setminus\Gamma}|\nabla u|^2dx+\frac{\eta}{2}\int_\Omega(f-u)^2dx, \tag{1.1}$$

where μ, η are two positive constants, $\mathcal{H}^1(\cdot)$ denotes the one-dimensional Hausdorff measure in $\mathbb{R}^2$, Γ is a compact curve in Ω, ∇ represents gradient operator, and $u:\Omega\to\mathbb{R}$ is an underlying piecewise smooth approximation of f. The latent image u is continuous or even derivable in $\Omega\setminus\Gamma$, whereas it is discontinuous across Γ. As aforementioned, Eq. (1.1) is nonsmooth and nonconvex, it is difficult to be solved efficiently. To overcome this shortcoming, some researchers proposed to utilize the discrete functionalities to approximate Eq. (1.1) [8,14,17] and achieve good segmentation results.

Furthermore, a simplified approach [15,16] of Eq. (1.1) has been proposed to improve the Mumford-Shah model. While ∇u is set to be zero identically on the domain $\Omega\setminus\Gamma$, it becomes the Mumford-Shah model with the piecewise constant. In [18], Chan and Vese proposed an active contours strategy without edges, which fixes the solution to be two piecewise constants (Chan-Vese model). However, Chan-Vese model cannot segment the images with intensity inhomogeneity or elongated structures well. Many models related to the Chan-Vese model were presented to solve this problem, we refer to see [19,20].

Recently, Cai, Chan and Zeng [21] proposed an image segmentation method based on the convex variant of the Mumford-Shah model and the thresholding strategy, which can be divided into two stages (TSMS). In the first stage, the authors found a smooth image u from the given image f. The smooth u can be obtained by solving the following total variation (TV) based model

$$\min_{u\in W^{1,2}(\Omega)}\int_\Omega|\nabla u|dx+\frac{\eta}{2}\int_\Omega(f-Au)^2dx+\frac{\mu}{2}\int_\Omega|\nabla u|^2dx, \tag{1.2}$$

where $W^{1,2}(\Omega)$ is the Sobolev space [22]. $u\in W^{1,2}(\Omega)$ is the clean image and A is a blurring or identity operator. In the second stage, a K-means method is applied to threshold the smoothed image obtained in the first stage. The two-stage strategy has been widely used for image segmentation. For example, Chan, Yang and Zeng [23] proposed a two-stage approach to segment the blurry images with Poisson or multiplicative Gamma noise. Duan et al. [24] extended the two-stage segmentation method by applying the Euler's Elastica regularization. Zhi, Sun and Pang [25] presented a two-stage image segmentation scheme based on the Inexact Alternating Direction Method. Ma, Peng and

Kong [26] introduced a mean curvature regularized Mumford-Shah model using a two-stage strategy. Chan, Yang and Zeng [27] proposed a two-stage segmentation method for variational Retinex. Li and Zeng [28] introduced a two-stage approach for multi-channel image segmentation. Wu et al. [29] proposed a two-stage image segmentation strategy based on the nonconvex L_2-L_p approximation of the Mumford–Shah model.

The variation-based models are an important kind of method developed in recent years [30–32]. Inspired by [21], we propose a two-stage image segmentation strategy based on the FBTV model [33]. The FBTV is a coupling of anisotropic and isotropic TV, which can be defined as $L_1-\alpha L_2$. It is a popular nonconvex relaxation method in image processing [33, 37–39]. Unlike the L_1-L_2 model in [40], the FBTV introduces a parameter α, which can maintain sharp edges and reduce the blocky artifacts. Furthermore, the FBTV considers the occurrence of non-sparse gradient vectors along the edges in the image [40], which is greatly significant in image processing. And we propose a DCA-based framework with sPADMM algorithm to solve the corresponding optimization problem, which is widely used to solve the nonconvex problem with several advantages: simplicity, inexpensiveness and efficiency [41]. The task of filling in missing or damaged regions of an image is known as image inpainting which has many important applications in the area of digital image processing, visual analysis and film industry [36]. Especially, unlike the models in [21, 23, 25–27], our model also considers the segmentation for the images with missing pixels. The main contributions of our work are as follows.

- Horizontal or vertical edges are more preferable in the FBTV model comparing with other TV models. Therefore, we present a segmentation model based on the FBTV. We use the FBTV as the regularization to detect the cartoon part of the given image.

- Since our model is nonconvex and nonsmooth, it is very challenging to solve this problem. Therefore, we design a strategy based on sPADMM algorithm to solve the TV-type subproblem in the DCA framework. To the best of our knowledge, sPADMM has not been considered to solve the subproblem in the DCA framework.

- To display the effectiveness of our segmentation method, we test the operator A in the TSMS model, which considers the segmentation of a variety of degradation cases (including noise, blur and missing pixels). Experiments show our proposed model and algorithm can have better performance.

The rest of this paper is organized as follows. In Section 2, we review the works of the FBTV. In Section 3, we propose our new two-stage strategy based on the FBTV. The DCA and sPADMM algorithms were employed to solve our model in Section 4. In Section 5, we discuss the implementation details and evaluation criteria, then devote ourselves to numerical experiments. Finally, the conclusions are given in Section 6.

2 Preliminaries and related works

2.1 Discrete gradient operator

The discrete gradient operator can be defined as $\nabla=(\nabla_x,\nabla_y)^T$, where ∇_x, ∇_y are the horizontal and vertical finite difference of the discrete image. For instance, we define

$$(\nabla_x u)_i=\begin{cases} u(1,1)-u(1,n), & i=1, \\ u(1,i)-u(1,i-1), & i=2,\cdots,n, \end{cases} \tag{2.1}$$

where n is the number of pixels of the first row of u and $u(1,i)$ is the i-th pixel of the first row of u. Similarly, we can define ∇_y.

2.2 Fischer-Burmeister total variation

The TV was widely used in the fields of image restoration, segmentation and related computer vision. Generally, the TV can be divided into two types: the isotropic and anisotropic TV. In [42], the isotropic TV was firstly proposed to protect the sharp edges of the image by Rudin et al., which was called ROF model. Then an anisotropic style was addressed in [43]. Let u be a column vector reshaped from a two-dimensional image, $J_1(u)$ and $J_2(u)$ denote the isotropic and anisotropic TV, respectively. $J_1(u)$ and $J_2(u)$ can be defined as

$$J_1(u):=\|\nabla u\|_{2,1}=\left\|\sqrt{|\nabla_x u|^2+|\nabla_y u|^2}\right\|_1, \tag{2.2a}$$

$$J_2(u):=\|\nabla u\|_1=\|\nabla_x u\|_1+\|\nabla_y u\|_1, \tag{2.2b}$$

where $\|\cdot\|_1$ represents the L_1 norm which is the sum of absolute values for a vector. It is noteworthy that Eq. (2.2) exploits the L_1-norm of the gradient of u instead of the $\mathcal{H}^1(\Gamma)$ term used in the Mumford-Shah model. Meanwhile, the regularity term is integrated into Ω in the Eq. (2.2) which takes the place of $\Omega\backslash\Gamma$. Hence, Eq. (2.2) has a unique smooth minimizer due to the convex property.

Let us introduce the Fischer-Burmeister (FB) function in scalar form. Denote ν_1 and ν_2 as real constants. Hence, scalar-valued FB function $\phi:\mathbb{R}\times\mathbb{R}\to\mathbb{R}$ is

$$\phi(\nu_1,\nu_2):=\nu_1+\nu_2-\sqrt{\nu_1^2+\nu_2^2}, \tag{2.3}$$

which is proposed by Fischer [44]. As FB function has some outstanding properties including strong semi-smoothness, it has been further studied in the nonlinear complementarity problem (NCP). The NCP is to obtain a vector $x\in\mathbb{R}^n$ so that

$$\psi(x)\geq 0,\quad x\geq 0,\quad \psi(x)^T x=0, \tag{2.4}$$

where $\psi:\mathbb{R}^n\to\mathbb{R}^n$ is the given vector-valued function. In this paper, a variant of FB function is defined as

$$\phi(\nu_1,\nu_2):=\nu_1+\nu_2-\theta\sqrt{\nu_1^2+\nu_2^2}, \tag{2.5}$$

where θ is a real constant.

The L_0 norm of the gradient $\|\nabla u\|_0$ can be regarded as the length of partition boundaries [45, 46]. However, the problem based on solving L_0 norm is NP-hard. To handle the L_0 norm, kinds of research adopted a convex method by using L_1 norm instead of L_0 norm on the gradient [47]. L_1 norm on the gradient is often called TV norm. In order to ensure the sparsity of L_1 norm, the restricted isometry property (RIP) is usually needed to be fulfilled [48]. Some nonconvex penalties methods to keep sparse solutions were proposed as alternatives to L_1 norm when violating the RIP condition, such as L_1-L_2 [40], L_p $(0<p<1)$ [49], transformed-L_1 [50] and capped-L_1 [51]. Thereinto, L_1-L_2 penalty is proved to be the good method, which forces the gradient ∇u to be horizontal or vertical. In [40], Lou et al. proved that L_1-L_2 is closer to L_0 than those of L_1. Illuminated by L_1-L_2 minimization [40,52], Lou et al. proposed $L_1-\alpha L_2$ model as a coupling of anisotropic and isotropic TV [33]

$$J(u)=J_1(u)-\alpha J_2(u)=\|\nabla_x u\|_1+\|\nabla_y u\|_1-\alpha\left\|\sqrt{|\nabla_x u|^2+|\nabla_y u|^2}\right\|_1, \tag{2.6}$$

where α is an element of the interval $(0,1]$ and is selected according to gradient distributions. When

$$\nu_1=\|\nabla_x u\|_1,\quad \nu_2=\|\nabla_y u\|_1,$$

Eq. (2.6) can be viewed as the application of FB function to the gradient of TV, so we call it FBTV. It was proved to be better than anisotropic or isotropic TV individually [33]. As the FBTV takes into account the non-sparse gradient vectors along the boundaries in the target image, it works particularly well for piecewise constant images comparing with other TV regularizations. Furthermore, unlike L_1-L_2 norm, FBTV considers other gradient directions, not just horizontal and vertical. It can control the influence of the anisotropic TV to detect sharp edges and reduce the blocky artifacts. Therefore, in this paper, we use the FBTV to replace the TV term in Eq. (1.2).

When using convex L_1 norm on the gradient, many algorithms have been developed, including the alternating minimization algorithm (AMA) [53], the augmented Lagrange multiplier (ALM) algorithm [54] and the alternating direction method of multipliers (ADMM) [55]. Since the $L_1-\alpha L_2$ is nonconvex and has two nonsmooth components, those popular optimization algorithms cannot generate a better result [56]. As a result, we need to seek help from other more general optimization algorithms. Since $L_1-\alpha L_2$ can be viewed as the difference between two convex functions, we naturally use the DCA to handle this problem. We will give more details about the DCA in Section 4.

3 FBTV-based segmentation method (FBTVS)

In this paper, we propose a two-stage image segmentation method based on the FBTV regularization, which is a variant of the related TSMS model proposed by Cai et al. [21].

3.1 The first stage of our method

In the first stage, we solve the smooth image u. Based on the analysis in Section 2.2, the FBTVS model struggles to minimize the following function

$$\min_u J(u)+\frac{\eta}{2}\|f-Au\|_2^2+\frac{\mu}{2}\|\nabla u\|_2^2. \tag{3.1}$$

The first term in Eq. (3.1) is the FBTV regularization term designed to preserve the features along the edges of the objective parts. The second term is the data fidelity term, which forces $f\approx Au$ while the last term is also a regularization term which controls the smoothing of the solution u. In this paper, we consider the more general problems in segmentation, which are embodied in the generalization of the operator A. For operator A, the different options of it correspond to the original images degraded by distinct corruptions:

- The input images with Gaussian noise only, i.e., $A=I$, I is an identity matrix;
- The input images with different kinds of blur and Gaussian noise, i.e., $A=B$, B is a liner blur operator;
- The input images with missing pixels only, i.e., $A=M$, M is a binary matrix which symbolizes missing pixels.

Our model uses the FBTV regularization, which can improve detection of sharp boundaries and avoid too many block artifacts. For numerical optimization, we can solve the Eq. (3.1) by utilizing the DCA-based method, which is a robust and popular method for nonconvex programming. The research indicates when properly stopped, the DCA iterations are usually close to the global minimum and yield great results.

3.2 The second stage of our method

In the second stage, we start with using the K-means method to ascertain the thresholds of the smooth image u. Once the proper thresholds have been confirmed, the segmentation can be obtained by segmenting u. Furthermore, we can change the thresholds or the number of phases of segmentation to given images without recomputing the problem in the first stage again.

4 Numerical algorithm

Since the nonconvex and nonsmooth of the minimization problem in Eq. (3.1), DCA-based methods can be used to solve it easily. In this section, we will apply the DCA with sPADMM to handle this problem. The proposed algorithm can solve nonconvex problems effectively.

4.1 Solving the Eq. (3.1) by DCA with sPADMM

The objective function in discrete form is as follows

$$\begin{aligned} Z(u)=&\|\nabla_x u\|_1+\left\|\nabla_y u\right\|_1+c\|u\|_2^2+\frac{\eta}{2}\|f-Au\|_2^2+\frac{\mu}{2}\|\nabla u\|_2^2\\ &-\alpha\left\|\sqrt{|\nabla_x u|^2+\left|\nabla_y u\right|^2}\right\|_1-c\|u\|_2^2. \end{aligned} \tag{4.1}$$

Here we highlight that as the problem is nonconvex and nonsmooth, several classical algorithms can not be used to solve it. Hence, we design a DCA-based algorithm with the sPADMM iteration, which is both fast and stable. Then, we separate $Z(u)$ into DC constituent in the following form, i.e., $Z(u)=z_1(u)-z_2(u)$, where

$$\begin{cases} z_1(u)=\|\nabla_x u\|_1+\left\|\nabla_y u\right\|_1+c\|u\|_2^2+\frac{\eta}{2}\|f-Au\|_2^2+\frac{\mu}{2}\|\nabla u\|_2^2,\\ z_2(u)=\alpha\left\|\sqrt{|\nabla_x u|^2+\left|\nabla_y u\right|^2}\right\|_1+c\|u\|_2^2, \end{cases} \tag{4.2}$$

and c is a positive constant to insure strong convexity between $z_1(u)$ and $z_2(u)$. After linearizing the $z_2(u)$, the minimization problem goes to the following form

$$\min_u \|\nabla_x u\|_1+\left\|\nabla_y u\right\|_1+c\|u\|_2^2-\alpha\langle\nabla u,q^n\rangle-2c\langle u,u^n\rangle+\frac{\eta}{2}\|Au-f\|_2^2+\frac{\mu}{2}\|\nabla u\|_2^2, \tag{4.3}$$

where

$$q^n=\frac{\left(\nabla_x u^n,\nabla_y u^n\right)}{\sqrt{|\nabla_x u^n|^2+\left|\nabla_y u^n\right|^2}}. \tag{4.4}$$

To be specific, we take the convention that if the denominator is zero at some points, the corresponding q^n value is intended to be zero.

The DCA subproblem in Eq. (4.3) equal to solving a TV type minimization problem and there are many methods used to solve the relevant TV problem, such as AMA [53], ALM [54], ADMM [55] and sPADMM [34]. Therein, AMA and ALM may not converge for this optimization problem. The ADMM has recently been used in various areas of scientific computing including optimization, image processing and machine learning [35]. However, sPADMM considers the global linear rate of convergence [34], which converges

at a higher speed than ADMM. Also, it performs well in figuring out potential insolubility issues of the subproblems and has a great capacity for solving the multi-block problems [34]. Therefore, we apply the sPADMM to find the smooth solution of the minimization problem in Eq. (4.3).

In the rest of the subsection, we will give a detailed introduction to the detailed sPADMM algorithm used in the model. To apply the sPADMM iteration, we introduce three auxiliary variables (d_x,d_y,z) to rewrite the original minimization problem (4.3) into the constrained form

$$\begin{aligned}\min_{\Theta}\|d_x\|_1+\|d_y\|_1+c\|u\|_2^2-\alpha\left(d_x^T\cdot q_x^n+d_y^T\cdot q_y^n\right)-2c\langle u,u^n\rangle\\ +\frac{\eta}{2}\|Az-f\|_2^2+\frac{\mu}{2}\|\nabla u\|_2^2,\qquad \text{s.t.}\quad d_x=\nabla_x u,\quad d_y=\nabla_y u,\quad z=u,\end{aligned}\tag{4.5}$$

where $\Theta=\{u,z,d_x,d_y;\,v,b_x,b_y\}$. Then, we apply the sPADMM iteration to enforce the constraints strictly. Based on the augmented Lagrangian method, three Lagrange multipliers are introduced into Eq. (4.5). Hence, we have an iterative scheme below

$$\begin{aligned}\Theta=\arg\min_{\Theta}\|d_x\|_1+\|d_y\|_1+c\|u\|_2^2-\alpha\left(d_x^T\cdot q_x^n+d_y^T\cdot q_y^n\right)\\ -2c\langle u,u^n\rangle+\frac{\mu}{2}\|Az-f\|_2^2+\frac{\eta}{2}\|\nabla u\|_2^2+\frac{\lambda_1}{2}\|d_x-\nabla_x u-b_x\|_2^2\\ +\frac{\lambda_1}{2}\|d_y-\nabla_y u-b_y\|_2^2+\frac{\lambda_2}{2}\|z-u-v\|_2^2,\end{aligned}\tag{4.6}$$

where b_x, b_y, v represent the Lagrange multipliers corresponding to the constraints $d_x=\nabla_x u$, $d_y=\nabla_y u$ and $z=u$, respectively. For notational convenience, we define

$$\Theta=\arg\min_{\Theta}\mathcal{L}(u,z,d_x,d_y;v,b_x,b_y).\tag{4.7}$$

Under the condition that Lagrange multipliers are given, the minimization of Eq. (4.6) can be solved by minimizing with respect to u and (d_x,d_y,z) alternatively. Hence, we need to solve the following minimization subproblems

$$\begin{cases}u^{n+1}=\arg\min_{u}\mathcal{L}(u,z^n,d_x^n,d_y^n;v^n,b_x^n,b_y^n)+\frac{1}{2}\|u-u^n\|_{S_1}^1,\\ z^{n+1}=\arg\min_{z}\mathcal{L}(u^{n+1},z,d_x^n,d_y^n;v^n,b_x^n,b_y^n)+\frac{1}{2}\|z-z^n\|_{S_2}^2,\\ d_x^{n+1}=\arg\min_{d_x}\mathcal{L}(u^{n+1},z^{n+1},d_x,d_y^n;v^n,b_x^n,b_y^n)+\frac{1}{2}\|d_x-d_x^n\|_{S_3}^3,\\ d_y^{n+1}=\arg\min_{d_y}\mathcal{L}(u^{n+1},z^{n+1},d_x^n,d_y;v^n,b_x^n,b_y^n)+\frac{1}{2}\|d_y-d_y^n\|_{S_4}^4,\end{cases}\tag{4.8}$$

where $\|x\|_S=\sqrt{\langle x,Sx\rangle}$ denotes the matrix norm for any $x\in\mathcal{X}$ and self-adjoint positive semi-definite linear operator S: $\mathcal{X}\to\mathcal{X}$. In particular, when $S_1=S_2=S_3=S_4=0$, sPADMM goes to be the ADMM.

A. u-subproblem.

The u-subproblem can be formulated as

$$u^{n+1}=\arg\min_u\left\{c\|u\|_2^2-2c\langle u,u^n\rangle+\frac{\eta}{2}\|\nabla u\|_2^2+\frac{\lambda_1}{2}\|d_x^n-\nabla_x u-b_x^n\|_2^2 + \frac{\lambda_1}{2}\left\|d_y^n-\nabla_y u-b_y^n\right\|_2^2+\frac{\lambda_2}{2}\|z^n-u-v^n\|_2^2+\frac{1}{2}\|u-u^n\|_{S_1}^2\right\}. \tag{4.9}$$

The Euler-Lagrange equation of which gives a linear equation shown as follows by taking the derivative

$$\begin{aligned}&[2cI+(\lambda_1+\eta)\nabla^T\nabla+\lambda_2+S_1]u^{n+1}\\ =&[\lambda_1\nabla_x^T(d_x^n-b_x^n)+\lambda_1\nabla_y^T\left(d_y^n-b_y^n\right)+\lambda_2(z^n-v^n)+2cu^n+S_1u^n].\end{aligned} \tag{4.10}$$

Under the periodic boundary condition for u, we know that $\nabla^T\nabla$, ∇_x^T and ∇_y^T are block circulants, the Hessian matrix on the left-hand of Eq. (4.10) can be diagonalized by two-dimensional discrete Fourier transform. Hence, the u-subproblem can be solved by utilizing the fast Fourier transform (FFT).

B. z-subproblem.

The z-subproblem can be described as

$$z^{n+1}=\arg\min_z\left\{\frac{\mu}{2}\|Az-f\|_2^2+\frac{\lambda_2}{2}\|z-u^{n+1}-v^n\|_2^2+\frac{1}{2}\|z-z^n\|_{S_2}^2\right\}, \tag{4.11}$$

which gives a linear equation

$$\left(\mu A^TA+\lambda_2 I+S_2\right)z^{n+1}=\mu A^Tf+\lambda_2(u^{n+1}+v^n)+S_2z^n. \tag{4.12}$$

The method of solving the above linear equation is depending on the operator A. When $A=I$ is an identity matrix or A is a blurring matrix, we can solve it by using the FFT method if operator A fulfills the periodic boundary condition. And if $A=M$ is a binary matrix, it can be solved directly.

C. (d_x,d_y)-subproblem.

The (d_x,d_y)-subproblem is indicated below

$$d_x^{n+1}=\arg\min_{d_x}\left\{\|d_x\|_1+\frac{\lambda_1}{2}\left\|d_x-\nabla_x u^{n+1}-b_x^n\right\|_2^2+\frac{1}{2}\|d_x-d_x^n\|_{S_3}^2-\alpha\left(d_x^T\cdot q_x^n\right)\right\}, \tag{4.13a}$$

$$d_y^{n+1}=\arg\min_{d_y}\left\{\left\|d_y\right\|_1+\frac{\lambda_1}{2}\left\|d_y-\nabla_y u^{n+1}-b_y^n\right\|_2^2+\frac{1}{2}\|d_y-d_y^n\|_{S_4}^2-\alpha\left(d_y^T\cdot q_y^n\right)\right\}. \tag{4.13b}$$

Denote sign$(\cdot)$ as the signum function. For the (d_x,d_y)-subproblem, it is solved by using the soft shrinkage formula defined as

$$d_x^{n+1}=\text{sign}(s_x^{n+1})\cdot\max\left\{\left|s_x^{n+1}-\frac{1}{\lambda_1+e_3}\right|,0\right\}, \tag{4.14a}$$

$$d_y^{n+1}=\text{sign}(s_y^{n+1})\cdot\max\left\{\left|s_y^{n+1}-\frac{1}{\lambda_1+e_4}\right|,0\right\}, \tag{4.14b}$$

where

$$s_x^{n+1}=(\lambda_1+e_3)^{-1}[\lambda_1(\nabla_x u^{n+1}+b_x^n)+\alpha q_x^n+S_3 d_x^n], \tag{4.15a}$$

$$s_y^{n+1}=(\lambda_1+e_4)^{-1}[\lambda_1(\nabla_y u^{n+1}+b_y^n)+\alpha q_y^n+S_4 d_y^n], \tag{4.15b}$$

e_3 and e_4 are the largest eigenvalues of the matrix S_3 and S_4, respectively.

D. Updating Lagrange multipliers.

In the end, the Lagrange multipliers (b_x,b_y,v) are updated as follows

$$\begin{cases} b_x^{n+1}=b_x^n+\sigma\lambda_1\left(\nabla_x u^{n+1}-d_x^{n+1}\right), \\ b_y^{n+1}=b_y^n+\sigma\lambda_1\left(\nabla_y u^{n+1}-d_y^{n+1}\right), \\ v^{n+1}=v^n+\sigma\lambda_2\left(u^{n+1}-z^{n+1}\right). \end{cases} \tag{4.16}$$

The above method leads to the first stage in Algorithm 4.1.

4.2 Mathematical analysis

4.2.1 Convergence analysis of DCA for our model

In this part, we give the proof of the existence and uniqueness of the minimizer of model (4.1).

We now prove that the sequence u^n got from (4.1) is convergent to a stationary point u^*. We reformulate our model as standard primal-dual model

$$\min_x\max_y\langle Lx,y\rangle-\mathcal{J}^*(q)+k(x), \tag{4.17}$$

where $x=u$, $y=q$, $L=\nabla$, $\mathcal{J}^*=\mathcal{X}^*$, where $\mathcal{X}^*$ is the characteristic function of the closed convex set, see [64]. And

$$k(x)=\frac{1}{2}\|x-x^n\|_{S_1}^2+\mathcal{L}(u,z,d_x,d_y;v,b_x,b_y).$$

Lemma 4.1. *The set of saddle points of problem* (4.17) *is non-empty.*

Proof. From [65, Theorem 4.3.1], if the conditions (H1)-(H4) in [65] are satisfied, then the saddle points set is non-empty. It is very straight-forward to prove that our model satisfies the above conditions. Then the saddle point of problem (4.17) exists. □

Theorem 4.1. *Assume that u^n is the sequence generated from DCA for solving* (4.1)*, then we have the following inequality*

$$Z(u^n)-Z(u^{n+1})\geq 0. \tag{4.18}$$

Proof. $a^n\in\partial z_1(u^n)$, from the definition of sub-differential, we have

$$z_1(u^{n+1})\geq z_1(u^n)+\left\langle u^{n+1}-u^n,a^n\right\rangle. \tag{4.19}$$

If u^n is the solution of problem (4.1), then $a^n\in\partial z_2(u^{n+1})$. Then we also have

$$z_2(u^n)\geq z_2(u^{n+1})+\left\langle u^n-u^{n+1},a^n\right\rangle. \tag{4.20}$$

Adding (4.19) and (4.20), we have

$$Z(u^n)-Z(u^{n+1})\geq 0. \tag{4.21}$$

Thus, we complete the proof. □

According to Lemma 4.1, the saddle point exists. Then we set u^n to be the solution of (4.17). For any n, $Z(u^n)\geq Z(u^*)$. Then we prove that $Z(u^n)$ is bounded below. From Theorem 4.1, $Z(u^n)$ is decreasing monotonically and bounded from below, thus convergent.

4.2.2 Convergence analysis of sPADMM for our model

In this part, we give the proof of the existence and uniqueness of the minimizer of model (4.3).

Lemma 4.2. *Suppose $f\in L^2(\Omega)$ and $Ker(\mathcal{A})\cap Ker(\nabla)=\{0\}$, where $\mathcal{A}$ is a bounded linear operator from $L^2(\Omega)$ to itself and $Ker(\mathcal{A})$. Then model* (4.3) *is strictly convex and there exists a unique minimizer $u(x)\in W^{1,2}(\Omega)$.*

Theorem 4.2. *Assume that $\{u^*,z^*,d_x^*,d_y^*,v^*,b_x^*,b_y^*\}$ is a Karush-Kuhn-Tucker (KKT) solution of formula* (4.3) *and the sequence $\{u^n,z^n,d_x^n,d_y^n,v^n,b_x^n,b_y^n\}$ is generated by the sPADMM. If $\sigma\in(0,\frac{1+\sqrt{5}}{2})$, then the sequence $\{u^n,z^n,d_x^n,d_y^n,v^n,b_x^n,b_y^n\}$ converges to an optimal solution of formula* (4.3)*.*

Proof. For formula (4.3), exactly follow [31] (Theorem 2.1 and Theorem 3.1), which has the same sPADMM framework used in this paper, and hence we omit the rest of the proof. □

4.3 Ascertaining the thresholds by K-means method

We emphasize that the FBTVS model in Eq. (3.1) can be solved with efficiency by using the DCA. Each DCA loop requires solving the TV type of minimization as a subproblem, which can be resolved by using the sPADMM. After smooth u is obtained, we utilize

the clustering method to confirm the segmented thresholds in the second stage. Without loss of generality, we normalize the pixels values of u to the interval $[0,1]$. To do the normalization, we use the linear-stretch formula defined as follows

$$\bar{u}=\frac{u-u_{\min}}{u_{\max}-u_{\min}}, \tag{4.22}$$

where $u_{\max}$ and $u_{\min}$ represent the maximum and minimum pixel of image u, respectively.

Recently, many clustering methods are proposed, such as K-means based methods [57–60], Fuzzy C-means (FCM) based methods [61–63]. In the following, we illustrate how to cluster a given set into K segments by the K-means method by an example, with K ascertained aforehand. Herein, we hypothesize $K\geq 2$. Denote $\hat{\rho}_1\leq\hat{\rho}_2\leq\cdots\leq\hat{\rho}_K$ are the mean values of K clusters, then we define the $K-1$ thresholds to be

$$\rho_i=\frac{\hat{\rho}_i+\hat{\rho}_{i+1}}{2},\quad i=1,2,\cdots,K-1. \tag{4.23}$$

The i-th phase of f $(1\leq i\leq K)$, then is given by $\{x\in\Omega:\rho_{i-1}<\bar{g}(x)\leq\rho_i\}$. To acquire the boundary of the i-th phase, the pixels in the i-th phase are set to be one while the others are set to be zero. Then we can use the MATLAB command "contour" to present them. Furthermore, the value of threshold ρ can be changed manually to get a preferable result. We need to underline that as u is calculated previously, then K and ρ are confirmed subsequently, we can debug the parameters of phases and thresholds without recomputing smooth solution u.

To sum up, a practical DCA-based numerical method is proposed to handle the FBTVS model (3.1) in the first stage, where the DCA-subproblem can be solved by using sPADMM. And in the second stage, to confirm the thresholds of the solution u, which is generated in the first stage, a K-means-based method is provided. The optimization procedure of the proposed is shown in Algorithm 4.1.

5 Numerical experiments

In this section, we present some numerical experiments to demonstrate the effectiveness of the proposed method and algorithm. We compare the proposed model with eight existing methods: Chan-Vese method [18], FRC method [66], TSMS method [21], CMF method [67], DPP method [12], EEMS method [24], ICTM method [68] and T-ROF method [69].

The Chan-Vese method is an active contour model based on Mumford–Shah segmentation techniques and the level set method [70]. The FRC uses fuzzy membership functions to approximate the piecewise constant Mumford-Shah model. The TSMS is a two-stage segmentation method based on the Mumford–Shah model for segmenting images (smoothing and thresholding), which is a classic TV model. The CMF proposes

Algorithm 4.1 DCA-sPADMM algorithm for FBTVS (here, Nmax and Kmax denote the maximum numbers of DCA and sPADMM iterations, respectively. And ϵ denotes the relative error of the sPADMM iteration).

Input: Give data f and choose parameters: η, μ, λ_1, λ_2, S_1, S_2, S_3, S_4, Nmax, Kmax.
Stage I:
Initialization: $u^0=0$, $d_x^0=d_y^0=z^0=0$.
for 1 to Nmax **do** $b_x^0=b_y^0=v^0=0$.
  for 1 to Kmax **do**
    Compute u^{n+1} by solving Eq. (4.10).
    Compute z^{n+1} by solving Eq. (4.12).
    Compute d_x^{n+1} and d_y^{n+1} by solving Eq. (4.14a).
    Update b_x^{n+1}, b_y^{n+1} and v^{n+1} by Eq. (4.16).
    if $\frac{\left\|u^{(n+1)}-u^{(n)}\right\|}{\left\|u^{(n+1)}\right\|}\leq\epsilon$, **then break**.
    end if
  end for
  Update q^{n+1} by Eq. (4.4).
end for
Stage II:
Choose K, determine the thresholds ρ by K-means method (or manually), and find the segmentations.
Output: Phases Ω_i, $i=1,\cdots,K$.

a graph cut based global minimization method for image segmentation by representing the segmentation label function with a series of nested binary super-level set functions. The DPP uses the dynamic programming and the ADMM algorithm to solve the Potts model which is non-convex. The EEMS modifies the Mumford-Shah model using Euler's Elastica as the regularization. A two-stage segmentation method is applied the Euler's Elastica regularized Mumford-Shah model. The ICTM is a new iterative convolution thresholding method including LIF, LSAC, and geodesic active contour models, which is suitable for image segmentation of a series of variational models. In this paper, we use the LIF model of the ICTM model to carry out the comparative experiment. The T-ROF explores a linkage between piecewise constant Mumford model and the ROF model, and derives a novel segmentation method, called thresholded-ROF (T-ROF) method, to illustrate the virtue of managing image segmentation through image restoration techniques. Methods in [12, 21, 24, 67–69, 72] are effective segmentation methods in or after 2013 and the codes used to perform the tests are provided by the authors. Compared with other models, our model has better stability and universality in different types. The parameters in the codes are selected through repeated works to give the results of each method as well as possible.

As analyzed in the previous section, our method can be divided into two stages: the first stage is to find a smooth solution u of the FBTV Mumford-Shah model by using DCA and sPADMM. After u is found, we select thresholds ρ to segment u. In our method, there are two ways to confirm the thresholds: the first is to use the MATLAB command "kmeans", which is a self-moving process; the second is to select ρ manually, which can refer to the thresholds ρ chosen by using the first method. During the rest of this article, ρ^K denotes the thresholds selected by MATLAB command "kmeans", and ρ^U denotes the thresholds chosen manually. Here we emphasize that we can get better results by adjusting the thresholds.

In the tests, we take into account three types of degraded images (i.e., noisy image, blurry image and the image with missing pixels), which are common in the real world. How to restore them has been further studied in recent years (see [71,73–75]). In the case of noise, we consider the Gaussian noise (GN), which is the most common noise in reality. It is implemented by the MATLAB command "imnoise". For the blurry cases, we take into account the four types of blur kernels (i.e., motion blur (MB), Gaussian blur (GB), average blur (AB) and disk blur (DB)), executing by the MATLAB command "fspecial". The specific form is displayed as follows.

- **Motion blur (MB):** fspecial('motion', LEN, THETA)
- **Gaussian blur (GB):** fspecial('gaussian', HSIZE, SIGMA)
- **Average blur (AB):** fspecial('average', HSIZE)
- **Disk blur (DB):** fspecial('disk', RADIUS)
- **Gaussian noise (GN):** imnoise(I, 'gaussian', MEAN, VARIANCE)

All the results were tested on PC with 2.50GHz CPU, 8GB RAM and MATLAB R2019b. And the boundaries of all results are shown on the given degraded images with color.

5.1 Evaluation criteria

In some cases, we utilize the intersection-over-union (IoU) [76, 77] to evaluate the segmentation results in an objective way. This metric is a method to quantify the percentage of overlap between the target mask and the prediction output. To be specific, the IoU metric measures the number of pixels common between the target and prediction masks divided by the total number of pixels present across both masks

$$\text{IoU} = (TP \cap PP)/(TP \cup PP), \tag{5.1}$$

where TP and PP represent the number of pixels of the target and prediction masks, respectively. The value of IoU is between $[0,1]$, and the closer these values are to 1, the better the segmentation is.

5.2 Parameters selection

In this subsection, the parameters setting in our algorithm will be discussed. Algorithm 4.1 has a outer DCA loop to update q and an inner loop to update u. The maximum numbers of outer and inner iterations are set to be 5 and 200 (i.e., $N\max = 5$, $K\max = 200$), and the minimum relative error ϵ for stopping the inner iteration satisfies the $\|u^{(n+1)} - u^{(n)}\| / \|u^{(n+1)}\| \leq 1 \times 10^{-4}$.

The parameters in this paper are set manually, which can make our results get a better IoU value. As shown in Fig. 1, it shows a parameter setting of Example 5.2. Figs. 1(a)-(d) show the variation curve of IoU value of parameter η, μ, λ_1 and λ_2 under different values, respectively.

The parameters η, μ, λ_1 and λ_2 are selected to obtain the best result. For parameter α, it can be shown from some researches that a larger value of α is possible to generate the nonsmooth u and a smaller α may remove much structure information from the recovered image. In this paper, we choose $\alpha = 0.5$. We choose the self adjoint positive

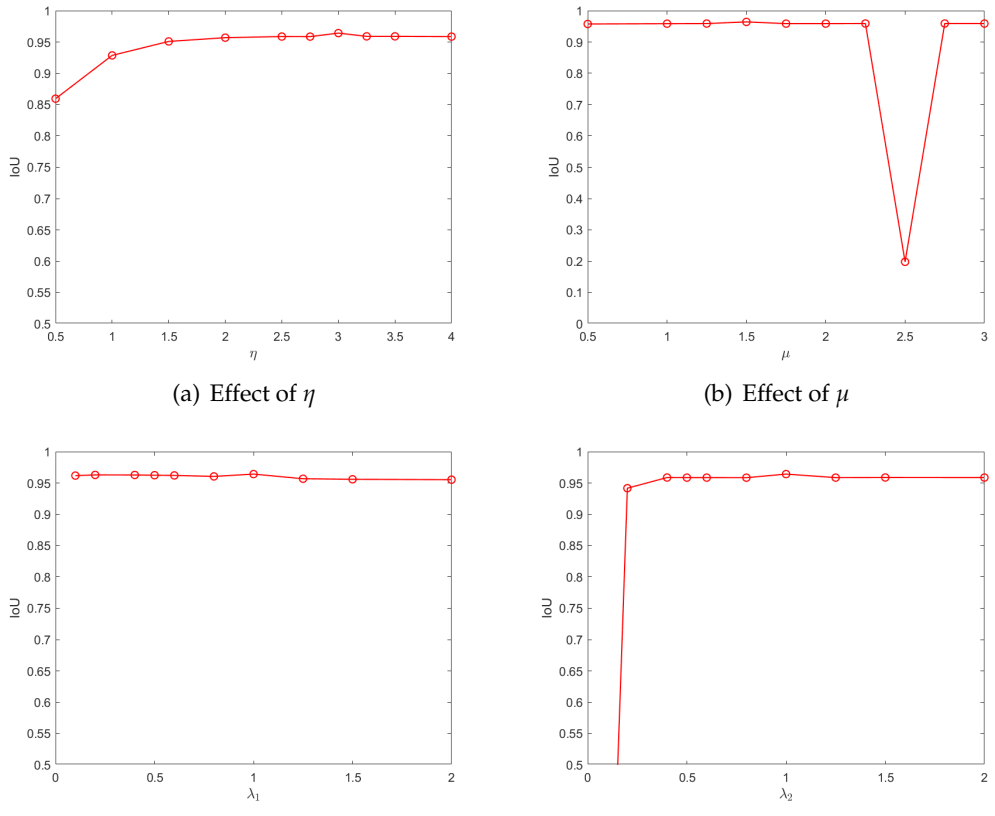

(a) Effect of η (b) Effect of μ

(c) Effect of λ_1 (d) Effect of λ_2

Figure 1: Sensitivity analysis with respect to parameters η, μ, λ_1 and λ_2 for Example 5.2.

semi-definite linear operators $S_1=S_2=S_3=S_4=\delta I$. To be specific, $\delta\in\{0.1,0.1,0.1,0.1\}$ for the case of noisy and/or blurry images, and $\delta\in\{0.1,0,0.3,0.4\}$ for the case of the images with missing pixels. Step size σ is selected to be 0.01.

In all experiments, according to the method in the paper, we adjust the parameters to the optimal value according to the following range [31]

a. Chan-Vese [18]: the regularization parameter $\lambda\in[0.1,1]$;

b. FRC [66]: the regularization parameter $\lambda\in[0.0001,1]$;

c. TSMS [21]: the regularization parameter $\lambda\in[0.1,1]$;

d. CMF [67]: the regularization parameter $\lambda\in[0.1,1]$;

e. DPP [12]: the regularization parameter $\lambda\in[0.1,5]$;

f. EEMS [24]: the regularization parameter $\lambda\in[0.1,1]$;

g. ICTM [68]: the regularization parameter $\lambda\in[100,500]$;

h. T-ROF [69]: the regularization parameter $\lambda\in[0.01,0.5]$.

5.3 The results of artificial images

Example 5.1 (Blurry and noisy image)**.** To prove our method does well on segmenting the blurry image, four images are shown in Figs. 2(a)-(d) are used, where each image

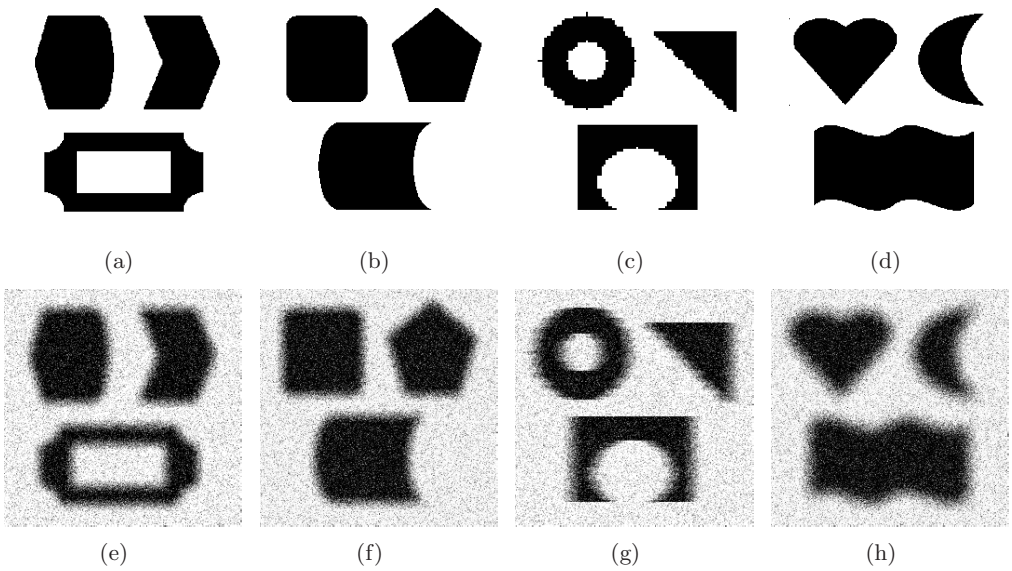

Figure 2: Testing images. (a)-(d) Clean images (256×256 pixels). (e)-(h) Corrupted images for (a)-(d) with GB, AB, MB and DB, respectively.

Table 1: IoU for blurry images segmentation (The best results in the simulation are given in bold.)

	Fig. 2(e)	Fig. 2(f)	Fig. 2(g)	Fig. 2(h)
Chan-Vese	0.9094	0.9576	0.9394	0.9323
FRC	0.9479	0.9690	0.9505	0.9542
TSMS	0.9572	0.9818	0.9343	0.9626
CMF	0.8626	0.9110	0.9507	0.8914
DPP	0.9437	0.9654	0.9516	0.9486
EEMS	0.9341	0.9676	0.9454	0.9491
ICTM	0.9166	0.9481	0.9380	0.9195
T-ROF	0.9590	0.9799	0.9564	0.9643
FBTVS using ρ^K	**0.9815**	**0.9881**	**0.9753**	**0.9697**
FBTVS using ρ^U	**0.9822**	**0.9884**	**0.9756**	**0.9703**

contains three geometric shapes. We test our method on four blurry images: Fig. 2(e) with GB, Fig. 2(f) with AB, Fig. 2(g) with MB and Fig. 2(h) with DB. In particular, we consider GB with HSIZE$=[15,15]$ and SIGMA$=20$, AB with HSIZE$=[15,15]$, MB with LEN$=20$ and THETA$=0$, DB with RADIUS$=12$. To make images more challenging to be segmented, we add a GN with MEAN$=0$ and VARIANCE$=0.04$ for all images. Herein, we only show the segmentation results of the case of GB. But for all blur cases, we will give the IoU of each group of experiments.

For GB, Fig. 3(k) is our solution u by using $\eta=10$, $\mu=10$, $\lambda_1=2$, $\lambda_2=4$. It is obvious that all the blur and the noise are clearly removed, which promotes the detection of the objects. Figs. 3(l) and (m) are our segmentation results with thresholds ρ^K and ρ^U, respectively. From the results, we can see that all the methods produce the segmentations similarly to our results with thresholds ρ^K and ρ^U, but our boundary depicts the shapes of the objects more precisely. By comparing the IoU shown in Table 1, it is clear that our method has higher IoU values than other methods, which indicates our method has better segmentation results of blurry and noisy images. And as can be seen from Table 1, we can manually change the thresholds to get better results of our method.

Example 5.2 (Multi-phase image with Gaussian noise)**.** To show the ability of our method in segmenting the multi-phase image, we test a four-phase artificial image with Gaussian noise. Figs. 4(a) and (b) show the clean and the given noisy images (for GN, we set MEAN=0 and VARIANCE=0.06), respectively. Fig. 4(g) is our smooth solution u when $\eta=1.5$, $\mu=3$, $\lambda_1=1$, $\lambda_2=1$. It is clear that our method reduces the noise very well. For the segmentation results of each method, we show each phase by using the mean value of the corresponding phase to represent the phase. Fig. 4(h) is our segmentation result with $\rho^K=(0.2454,0.4923,0.7796)$. Figs. 4(i)-(l) are the contours of the four phases by using our method. From Fig. 4, we see that TSMS, T-ROF and our method produce the boundaries which successfully segment each portion of the multi-phase image. However, FRC can not separate the third and the fourth phases correctly, and CMF can not separate the first and the second phases correctly. Fig. 5 is the convergence curve of relative error solved by

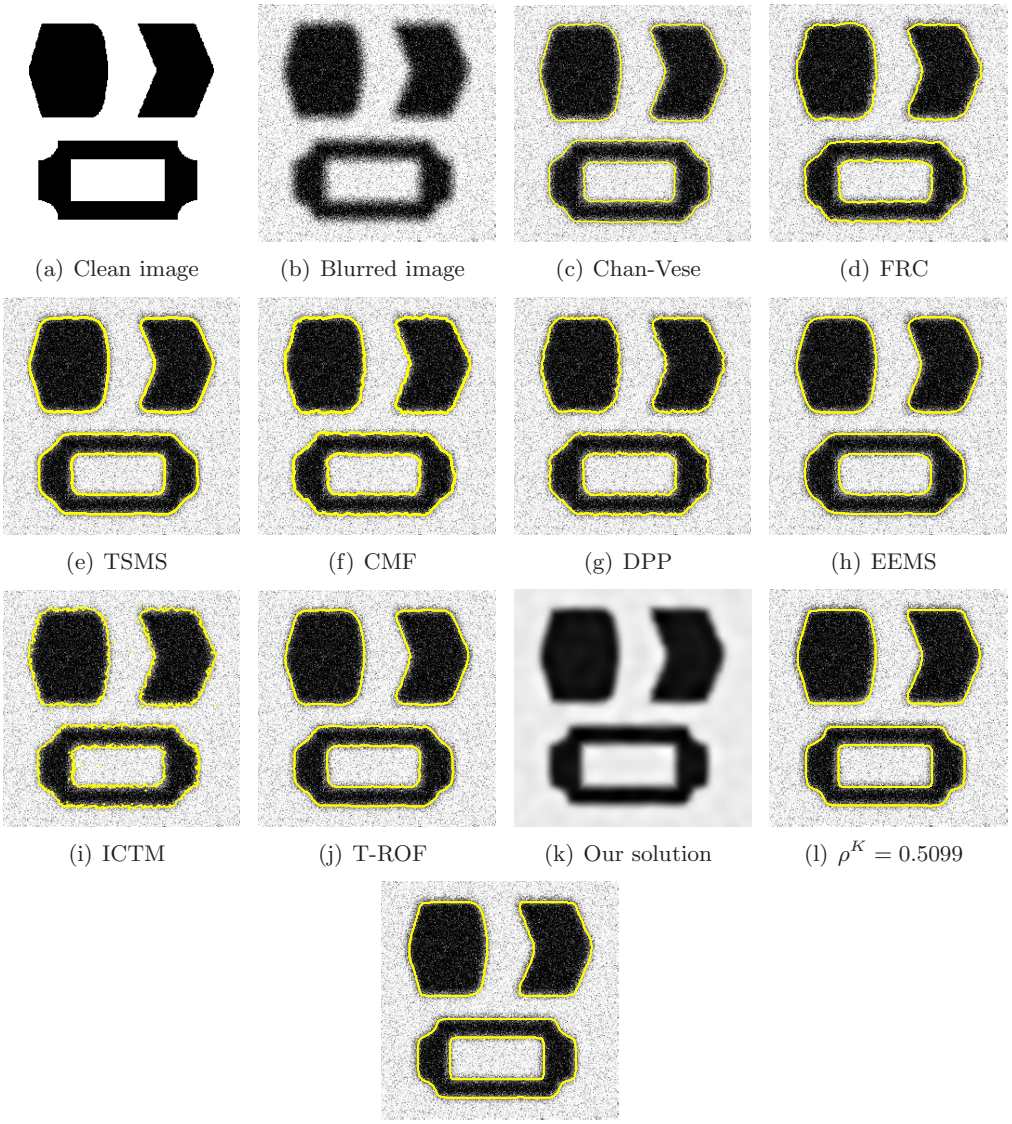

(a) Clean image (b) Blurred image (c) Chan-Vese (d) FRC

(e) TSMS (f) CMF (g) DPP (h) EEMS

(i) ICTM (j) T-ROF (k) Our solution (l) $\rho^K = 0.5099$

(m) $\rho^U = 0.5015$

Figure 3: The image with Gaussian blur. (a) Clean image (256×256 pixels). (b) Given blurry image with noise. (c)-(j) The results of Chan-Vese, FRC, TSMS, CMF, DPP, EEMS, ICTM and T-ROF. (k) Our solution u. (l) Our result using threshold $\rho^K = 0.5099$. (m) Our result using threshold $\rho^U = 0.5015$.

ADMM algorithm and sPADMM algorithm in Example 5.2. As can be seen from Fig. 5, compared with ADMM algorithm, sPADMM algorithm can quickly converge to a certain value 5×10^{-4}.

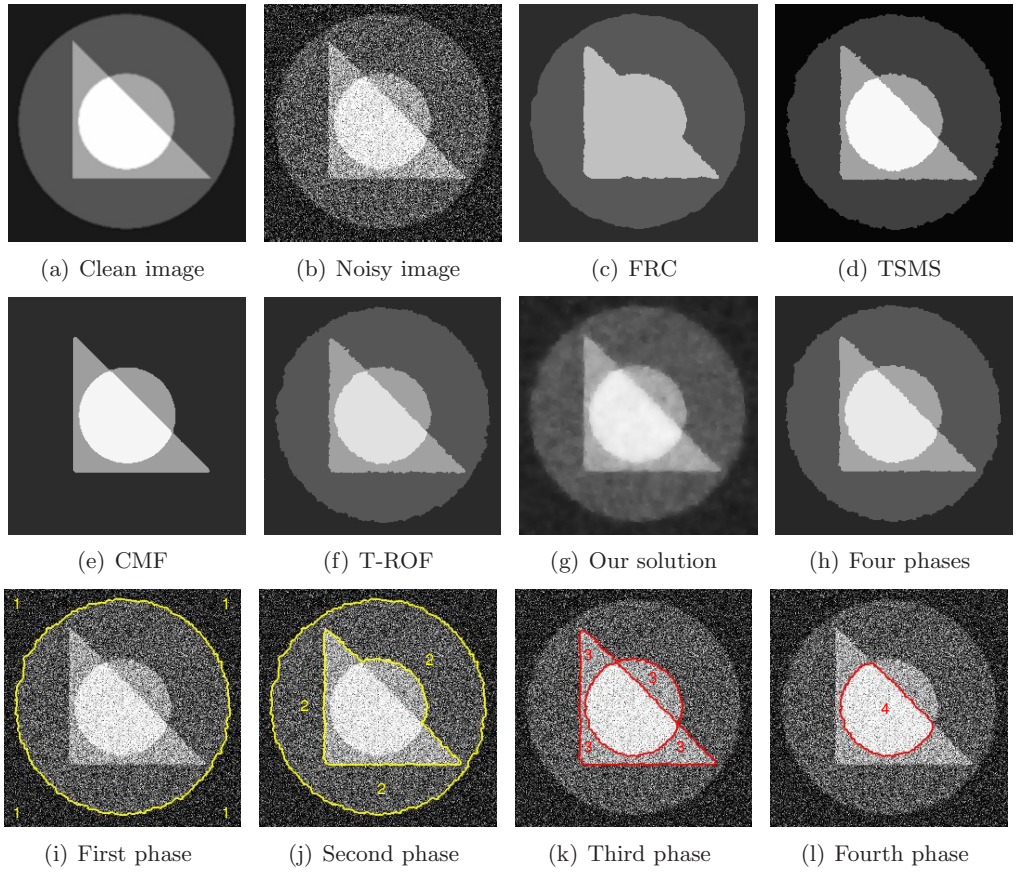

(a) Clean image (b) Noisy image (c) FRC (d) TSMS

(e) CMF (f) T-ROF (g) Our solution (h) Four phases

(i) First phase (j) Second phase (k) Third phase (l) Fourth phase

Figure 4: Four-phase artificial image. (a) Clean image (256×256 pixels). (b) Given image with Gaussian noise. (c)-(f) The results of FRC, TSMS, CMF and T-ROF. (g) Our solution u. (h) Our result using thresholds $\rho_1=0.2454$, $\rho_2=0.4923$ and $\rho_3=0.7796$. (i)-(l) Contours of each phase in (h).

5.4 The results of real images

Example 5.3 (Real brain image)**.** In this test, Fig. 6(a) is a given real brain image. The boundaries of some brain tissue are blurry and vague, as a result, they are hard to detect. Fig. 6(j) is our solution u by using $\eta=30$, $\mu=110$, $\lambda_1=2$, $\lambda_2=1.5$. Figs. 6(k) and (l) are our segmentation results by using thresholds $\rho^K=0.3420$ and $\rho^U=0.2300$, respectively. Comparing our results with the results from other state-of-the-art methods in Figs. 6(b)-(l), we see that other methods all generate similar results to our method by using ρ^K, while our method by using ρ^U obtains the best result, which nearly detects the whole brain tissue. In particular, it can detect where the arrow marks in Fig. 6(l).

Example 5.4 (Real plane image)**.** In this test, a real plane image shown in Fig. 7(a) is used. This image is challenging to be segmented for two reasons: the cloud has varying intensities, and there are some unclear boundaries between the rear wing and the pro-

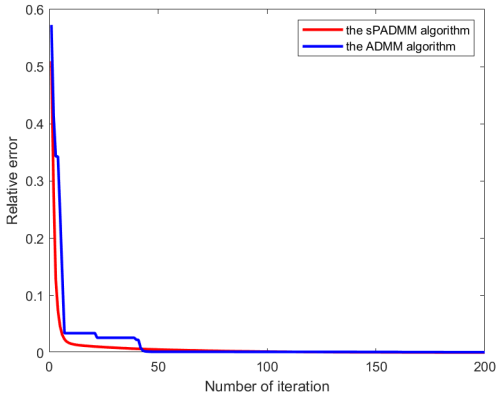

Figure 5: Relative error diagram of Example 5.2.

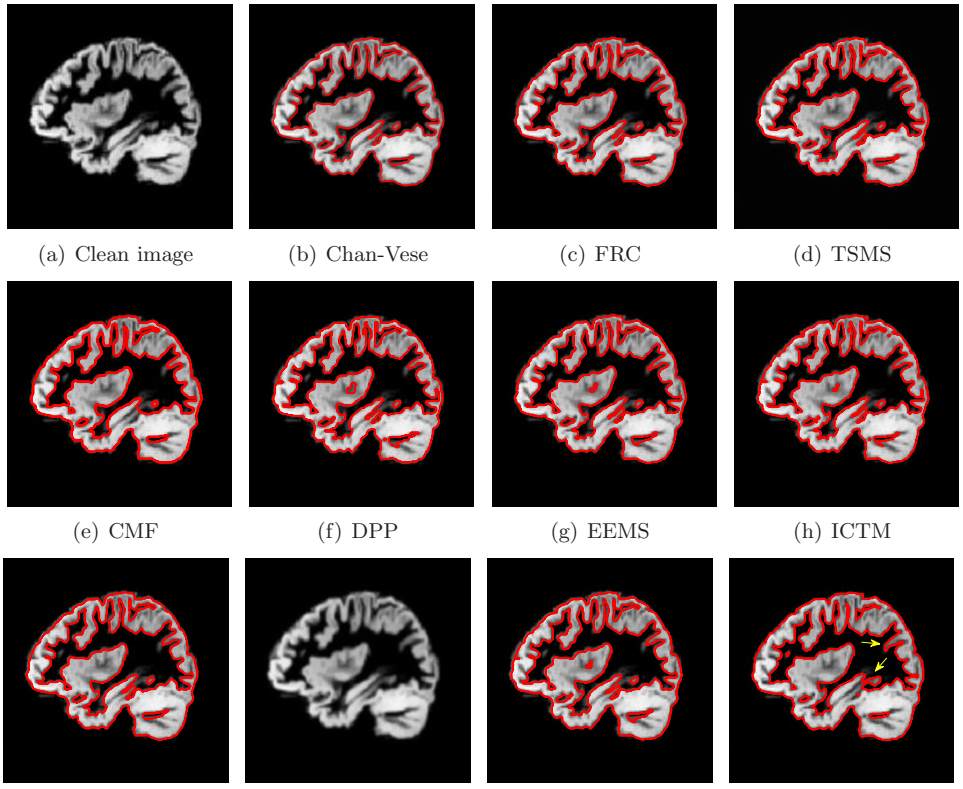

(a) Clean image (b) Chan-Vese (c) FRC (d) TSMS

(e) CMF (f) DPP (g) EEMS (h) ICTM

(i) T-ROF (j) Our solution (k) $\rho^K = 0.5166$ (l) $\rho^U = 0.3420$

Figure 6: Real brain image. (a) Clean image (256×256 pixels). (b)-(i) The results of Chan-Vese, FRC, TSMS, CMF, DPP, EEMS, ICTM and T-ROF. (j) Our solution u. (k) Our result using threshold $\rho^K = 0.3420$. (l) Our result using threshold $\rho^U = 0.2300$.

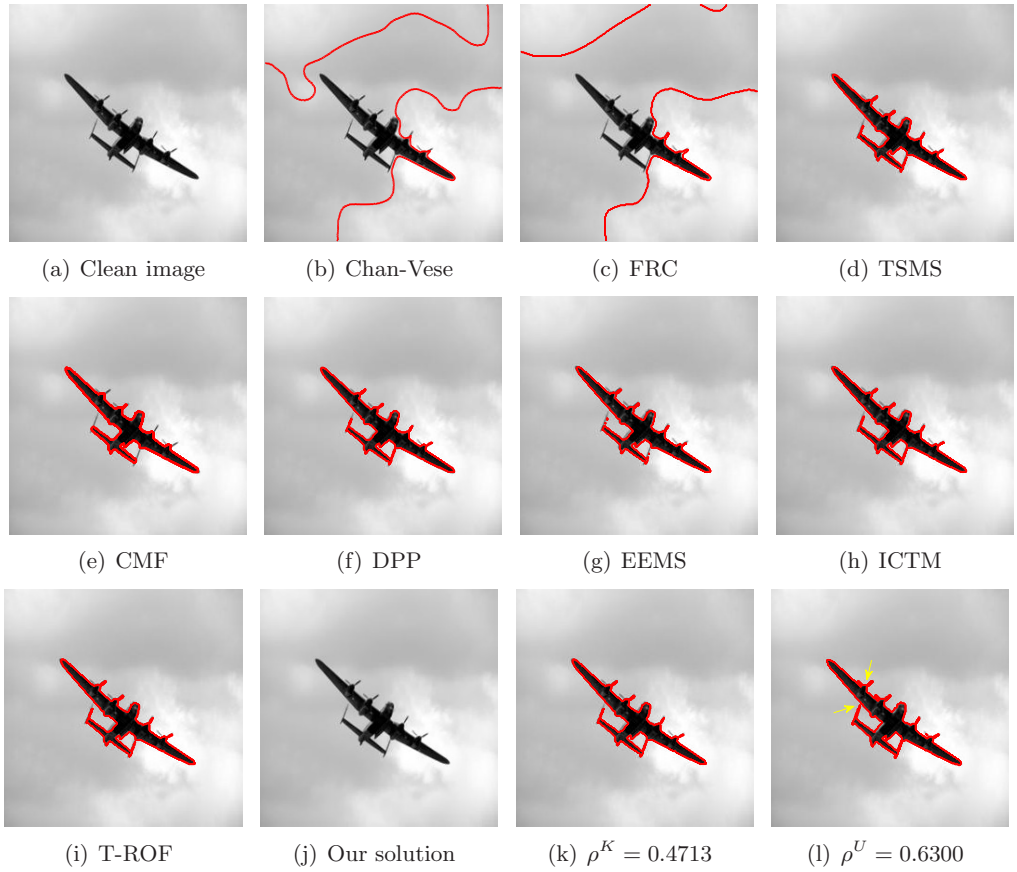

(a) Clean image (b) Chan-Vese (c) FRC (d) TSMS

(e) CMF (f) DPP (g) EEMS (h) ICTM

(i) T-ROF (j) Our solution (k) $\rho^K = 0.4713$ (l) $\rho^U = 0.6300$

Figure 7: Real plane image. (a) Clean image (256×256 pixels). (b)-(i) The results of Chan-Vese, FRC, TSMS, CMF, DPP, EEMS, ICTM and T-ROF. (j) Our solution u. (k) Our result using threshold $\rho^K=0.4713$. (l) Our result using threshold $\rho^U=0.6300$.

peller. The target of this test is to segment the whole plane as a single target, without containing pixels of the cloud. Fig. 7(j) shows our solution u when $\eta=1$, $\mu=155$, $\lambda_1=10$, $\lambda_2=10$. Figs. 7(k) and (l) are our final results by using thresholds ρ^K and ρ^U, respectively. As shown in Figs. 7(b) and (c), the results of Chan-Vese and FRC include large portions which are not the plane. Figs. 7(e) and (g) from CMF and EEMS can not segment the rear wing well. And TSMS, DPP, ICTM and T-ROF produce similar results with our method using threshold ρ^K; see Figs. 7(d), (f), (h) and (i). From Fig. 7(l), it is clear that we can modulate the threshold manually to obtain better results, e.g., see the arrow in Fig. 7(l).

Example 5.5 (Real cell image with high noise)**.** We conduct this test with the purpose of proving that our method can be applied well to the segmentation of the real image with high noise. We consider the GN with MEAN 0 and VARIANCE 0.5. Figs. 8(a) and (b) display the clean and the noisy images, respectively. Fig. 8(k) is our solution u obtained

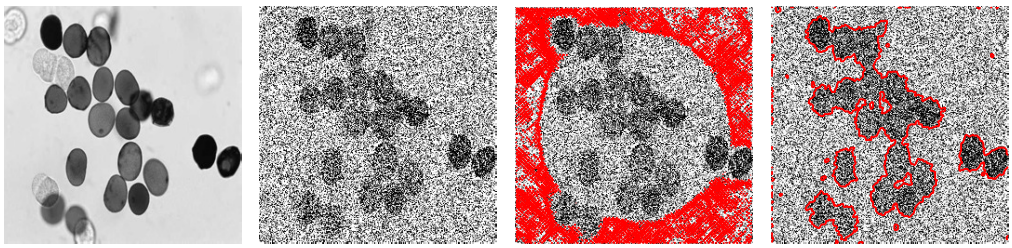

(a) Clean image (b) Noisy image (c) Chan-Vese (d) FRC

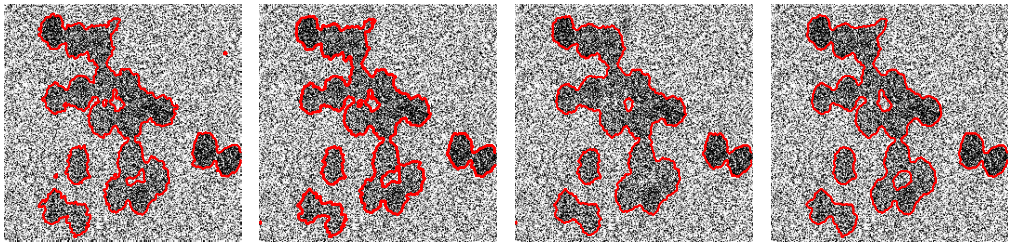

(e) TSMS (f) CMF (g) DPP (h) EEMS

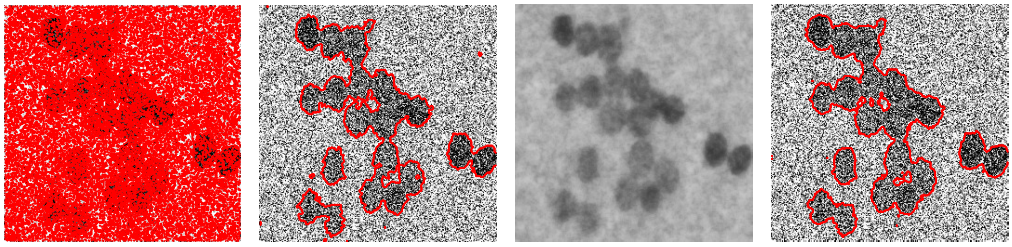

(i) ICTM (j) T-ROF (k) Our solution (l) $\rho^K = 0.5514$

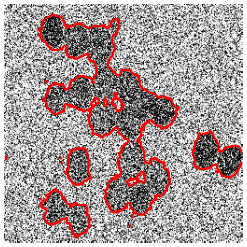

(m) $\rho^U = 0.5530$

Figure 8: Real cell image with high noise. (a) Clean image (256×256 pixels). (b) Given image with Gaussian noise. (c)-(j) The results of Chan-Vese, FRC, TSMS, CMF, DPP, EEMS, ICTM and T-ROF. (k) Our solution u. (l) Our segmentation result using threshold $\rho^K = 0.5514$. (m) Our segmentation result using threshold $\rho^U = 0.5530$.

by using $\eta = 50$, $\mu = 7$, $\lambda_1 = 2$, $\lambda_2 = 4$. Figs. 7(l) and (m) are our results by using thresholds ρ^K and ρ^U, respectively. From Figs. 8(c) and (i), we see that Chan-Vese and ICTM fail to detect the cells. Fig. 8(d) from FRC includes too many wrong boundaries due to the high noise. As shown in Fig. 8(g), we see that the cells are not separated well by DPP. From

Fig. 8, it is clear that TSMS, EEMS and T-ROF produce similar results to our method using thresholds ρ^K and ρ^U.

5.5 The results of images with missing pixels

Example 5.6 (Images with missing pixels)**.** Finally, we consider the image decomposition on two grayscale images with some missing pixels. Herein, we assume that for a binary matrix, the element where the value is zero represents the missing pixel. In this case,

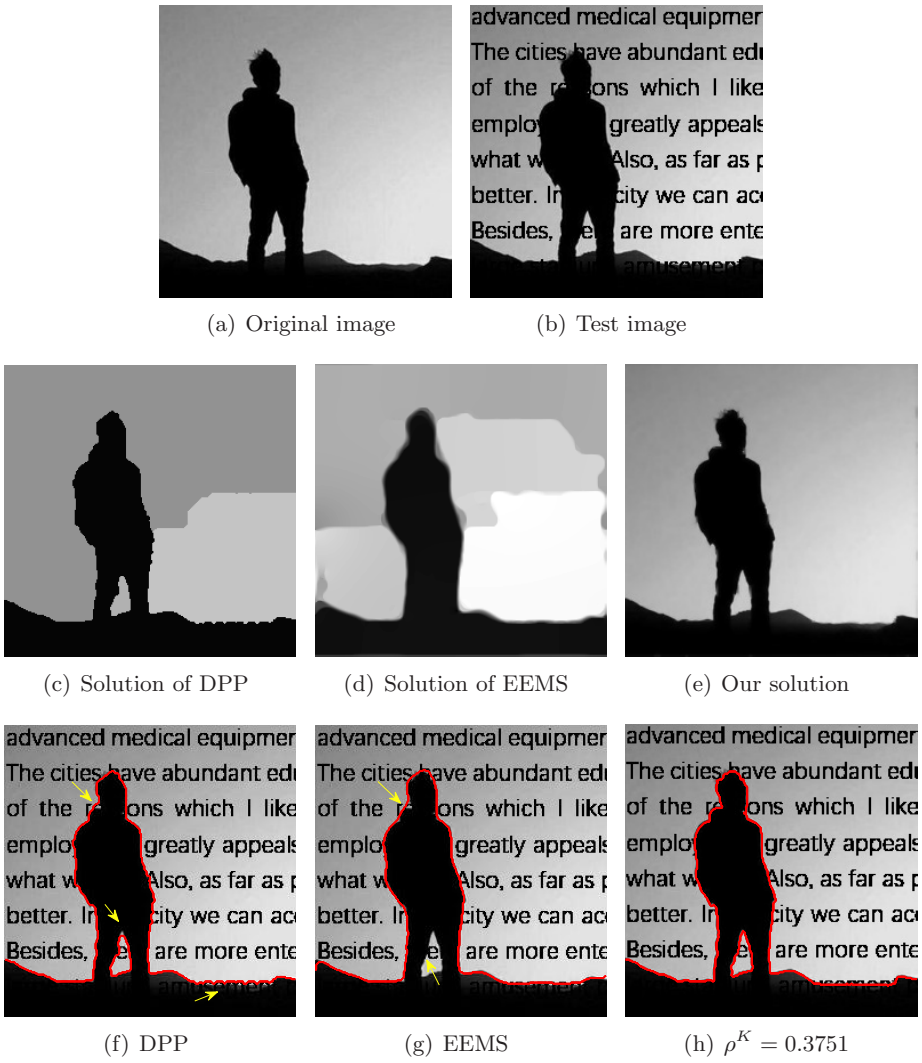

(a) Original image (b) Test image

(c) Solution of DPP (d) Solution of EEMS (e) Our solution

(f) DPP (g) EEMS (h) $\rho^K = 0.3751$

Figure 9: Human image with missing pixels. (a) Original images (256×256 pixels). (b) Given image with missing pixels. (c)-(e) Solutions of DPP, EEMS and our method. (f)-(h) The results of DPP, EEMS and our method.

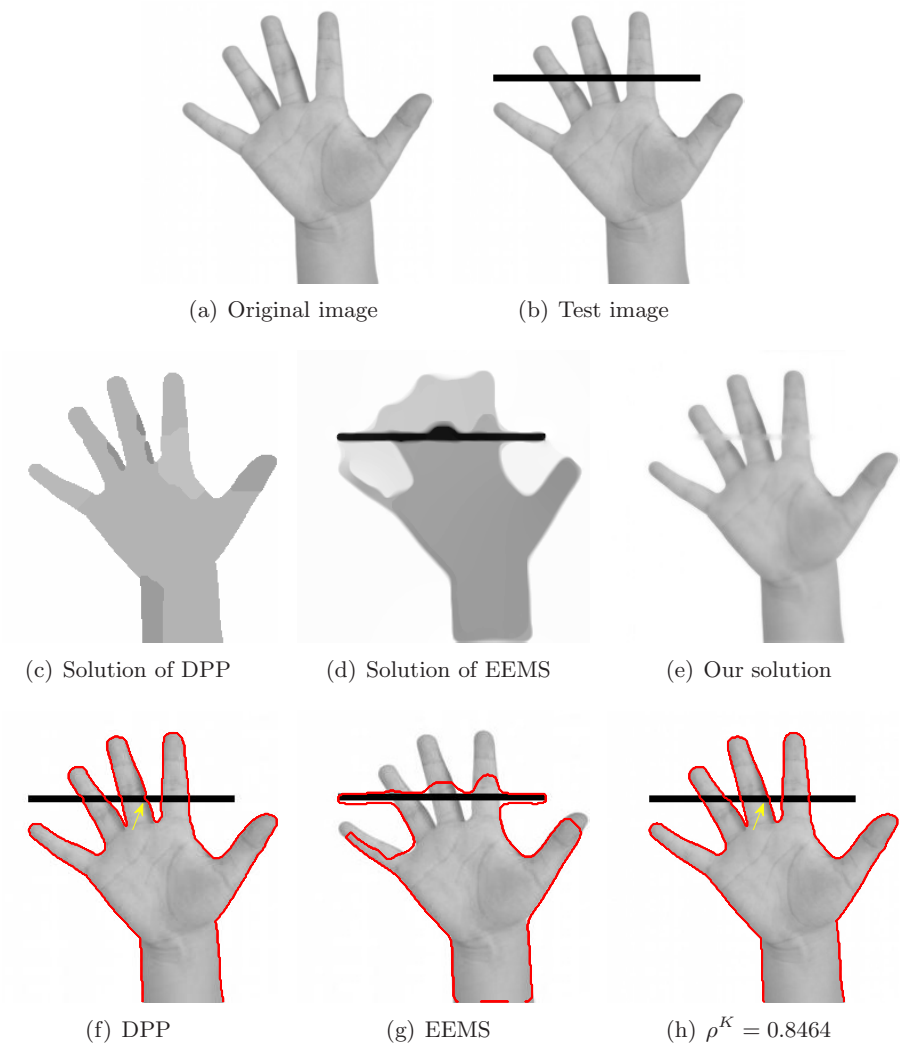

(a) Original image (b) Test image

(c) Solution of DPP (d) Solution of EEMS (e) Our solution

(f) DPP (g) EEMS (h) $\rho^K = 0.8464$

Figure 10: Hand image with missing pixels. (a) Original images (256×256 pixels). (b) Given image with missing pixels. (c)-(e) Solutions of DPP, EEMS and our method. (f)-(h) The results of DPP, EEMS and our method.

we first test Fig. 9(b) to illustrate that our method is well-performed in segmenting the image with missing pixels, where Fig. 9(a) is the original image. For the test, we only implement DPP, EEMS and our proposed model. In order to obtain our solution u shown in Fig. 9(e), we set $\eta=2$, $\mu=25$, $\lambda_1=2$, $\lambda_2=4$. From Figs. 9(c)-(e), we see that our smooth solutions are close to the original images, while EEMS produces the worst smooth solutions, which seriously impede the segmentation in the second stage. The thresholds used in the second stage are obtained from the MATLAB command "kmeans" automatically. As shown in Fig. 9(f), it is clear that DPP segments the object as a whole, but it also in-

cludes some incorrect parts in the segmentation, where the arrows in Fig. 9(f) indicate the wrong boundary. Fig. 9(g) from EEMS fails to detect well the boundary of the human, especially where the arrow marks. In contrast, our method recovers the object almost exactly; see Fig. 9(h).

Then, Fig. 10(b) is used to conduct the test. In this test, the parameters used in our method are the same as the previous test. After we obtain the smooth solution, the threshold is selected by MATLAB command "kmeans". As displayed in Figs. 10(c)-(h), it is clear that EEMS fails to restore the missing pixels, while DPP and our method not only eliminate the influence of missing pixels but also get successful results. However, our method generates a better result than DPP (please refer to the arrows in Figs. 10(f) and (h)).

6 Conclusions

In this paper, a two-stage image segmentation method based on the FBTV and thresholding is proposed. In the first stage, we apply the FBTV regularized Mumford-Shah model to find a smooth solution u. The proposed model has the advantages of maintaining sharp edges and reducing the blocky artifacts for segmentation. Moreover, our model can be used to segment the images with noise or/and blur, or even with missing pixels. To solve our model, we design a new DCA-based algorithm with the sPADMM iteration. It can solve the nonconvex and nonsmooth problems effectively. In the second stage, we use the thresholding segmentation strategy with proper thresholds given manually. It should be emphasized again that there is no need to recompute the smooth solution when we change the thresholds. The numerical results show that our method performs well in two-phase and multi-phase segmentation and can be applied to many kinds of corrupted images.

Acknowledgements

The research was supported by the Natural Science Foundation of China (Grant Nos. 61971234, 11501301, and 62001167), the "1311 Talent Plan" of NUPT, the "QingLan" Project for Colleges and Universities of Jiangsu Province, East China Normal University through startup funding, and Technology Innovation Training Program (Grant No. SZDG2019030).

References

[1] Q. Ge, L. Xiao, and Z. H. Wei, *Active contour model for simultaneous MR image segmentation and denoising,* Digital Signal Process., 23(4) (2013), pp. 1186–1196.

[2] P. Ruiz, N. P. De La Blanca, R. Molina, and A. K. Katsaggelos, *Bayesian classification and active learning using lp-priors. application to image segmentation,* in: 2014 22nd European Signal Processing Conference (EUSIPCO), IEEE (2014), pp. 1183–1187.

[3] Y. LIU, C. HE, AND Y. WU, *Variational model with kernel metric-based data term for noisy image segmentation,* Digital Signal Process., 78 (2018), pp. 42–55.
[4] F. FUENTES-HURTADO, V. NARANJO, J. A. DIEGO-MAS, AND M. ALCANIZ, *A hybrid method for accurate iris segmentation on at-a-distance visible-wavelength images,* Eurasip J. Image Video Process., 1 (2019), 75.
[5] C. WU, AND Z. KANG, *Robust entropy-based symmetric regularized picture fuzzy clustering for image segmentation,* Digital Signal Process., (2020), 102905.
[6] J. WANG, Z. XU, Z. PAN, W. WEI, AND G. WANG, *The vese-chan model without redundant parameter estimation for multiphase image segmentation,* Eurasip J. Image Video Process., 1 (2020), pp. 1–17.
[7] S. LUO, X.-C. TAI, AND Y. WANG, *Convex shape representation with binary labels for image segmentation: models and fast algorithms,* (2020), arXiv:2002.09600.
[8] D. MUMFORD, AND J. SHAH, *Optimal approximations by piecewise smooth functions and associated variational problems,* Commun. Pure Appl. Math., 42(5) (1989), pp. 577–685.
[9] A. CHAMBOLLE, *Finite-differences discretizations of the mumford-shah functional,* ESAIM: Math. Model. Numer. Anal., 33(2) (1999), pp. 261–288.
[10] T. F. CHAN, AND L. A. VESE, *A level set algorithm for minimizing the mumford-shah functional in image processing,* in: Proceedings IEEEWorkshop on Variational and Level Set Methods in Computer Vision, IEEE (2001), pp. 161–168.
[11] S. ESEDOG, AND Y.-H. R. TSAI ET AL., *Threshold dynamics for the piecewise constant mumford–shah functional,* J. Comput. Phys., 211(1) (2006), pp. 367–384.
[12] M. STORATH, AND A. WEINMANN, *Fast partitioning of vector-valued images,* SIAM J. Imag. Sci., 7(3) (2014), pp. 1826–1852.
[13] C. LIU, M. K.-P. NG, AND T. ZENG, *Weighted variational model for selective image segmentation with application to medical images,* Pattern Recognition, 76 (2018), pp. 367–379.
[14] G. AUBERT, L. BLANC-FERAUD, AND *R. March, An approximation of the mumford–shah energy by a family of discrete edge-preserving functionals,* Nonlinear Anal. Theory Methods Appl., 64(9) (2006), pp. 1908–1930.
[15] M. GENCTAV, AND S. TARI, *Multi-parameter Mumford-Shah segmentation,* Res. Shape Anal., (2018), pp. 133–141.
[16] Y. LI, C.WU, AND Y. DUAN, *The TV_p regularized Mumford-Shah model for image labeling and segmentation,* IEEE Trans. Image Process., 29 (2020), pp. 7061–7075.
[17] M. MORINI, AND M. NEGRI, *Mumford–shah functional as γ-limit of discrete perona–malik energies,* Math. Models Methods Appl. Sci., 13(6) (2003), pp. 785–805.
[18] T. F. CHAN, AND L. A. VESE, *Active contours without edges,* IEEE Trans. Image Process., 10(2) (2001), pp. 266–277.
[19] H. WANG, T.-Z. HUANG, AND J. LIU, *An efficient operator splitting method for local region chan-vese model,* Eurasip J. Adv. Signal Process., 2013 (2013), pp. 1–12.
[20] E. BAE, X.-C. TAI, AND Z. WEI, *Augmented lagrangian method for an euler's elastica based segmentation model that promotes convex contours,* American Institute of Mathematical Sciences, 11(1) (2017), pp. 1–23.
[21] X. CAI, R. CHAN, AND T. ZENG, *A two-stage image segmentation method using a convex variant of the mumford–shah model and thresholding,* SIAM J. Imag. Sci., 6(1) (2013), pp. 368–390.
[22] H. LEVINE, *Partial differential equations,* American Mathematical Society, 1997.
[23] R. CHAN, H. YANG, AND T. ZENG, *A two-stage image segmentation method for blurry images with poisson or multiplicative gamma noise,* SIAM J. Imag. Sci., 7(1) (2014), pp. 98–127.
[24] Y. DUAN, W. HUANG, J. ZHOU, H. CHANG, AND T. ZENG, *A two-stage image segmentation*

method using euler's elastica regularized mumford-shah model, in: 22nd International Conference on Pattern Recognition, IEEE, 2014, pp. 118–123.

[25] Z. ZHI, Y. SUN, AND Z.-F. PANG, *Two-stage image segmentation scheme based on inexact alternating direction method,* Numer. Math. Theory Methods Appl., 9(3) (2016), pp. 451–469.

[26] Q. MA, J. PENG, AND D. KONG, *Image segmentation via mean curvature regularized mumford-shah model and thresholding,* Neural Process. Lett., 48(2) (2018), pp. 1227–1241.

[27] R. CHAN, H. YANG, AND T. ZENG, *Total variation and tight frame image segmentation with intensity inhomogeneity,* (2019), arXiv preprint arXiv:1904.01760.

[28] Z. LI, AND T. ZENG, *A two-stage image segmentation model for multi-channel images,* Commun. Comput. Phys., 19(4) (2016), pp. 904–926.

[29] T. WU, J. SHAO, X. GU, M. K. NG, AND T. ZENG, *Two-stage image segmentation based on nonconvex l_2-l_p approximation and thresholding,* Appl. Math. Comput., 403 (2021), 126168.

[30] X. YANG,AND Y. HUANG, *A Modulus iteration method for SPSD linear complementarity problem arising in image retinex,* Adv. Appl. Math. Mech., 12 (2020), pp. 579–598.

[31] T. WU, X. GU, Y. WANG, AND T. ZENG, *Adaptive total variation based image segmentation with semi-proximal alternating minimization,* Signal Process., 183 (2021), 108017.

[32] T. WU, X. GU, J. SHAO, R. ZHOU, AND Z. LI, *Colour image segmentation based on a convex K-means approach,* IET Image Process., 2021.

[33] Y. LOU, T. ZENG, S. OSHER, AND J. XIN, *A weighted difference of anisotropic and isotropic total variation model for image processing,* SIAM J. Imag. Sci., 8(3) (2015), pp. 1798–1823.

[34] D. HAN, D. SUN, AND L. ZHANG, *Linear rate convergence of the alternating direction method of multipliers for convex composite programming,* Math. Operations Res., 43(2) (2018), pp. 622–637.

[35] T. WU, Z. PANG, Y. WANG AND Y. YANG, *CS-MRI reconstruction based on the constrained TGV-shearlet scheme,* Int. J. Numer. Anal. Model., 17(3) (2020), pp. 316–331.

[36] M. WANG, C. HUANG, C. ZENG, AND C. LAI, *Two-phase image inpainting: combine edge-fitting with PDE inpainting,* Adv. Appl. Math. Mech., 4 (2012), pp. 769–779.

[37] Y. LOU, P. YIN, AND J. XIN, *Point source super-resolution via non-convex L_1 based methods,* J. Sci. Comput., 68(3) (2016), pp. 1082–1100.

[38] T.-H. MA, Y. LOU, AND T.-Z. HUANG, *Truncated l_{1-2} models for sparse recovery and rank minimization,* SIAM J. Imag. Sci., 10(3) (2017), pp. 1346–1380.

[39] H. GE, J. WEN, AND W. CHEN, *The null space property of the truncated l_{1-2}-minimization,* IEEE Signal Process. Lett., 25(8) (2018), pp. 1261–1265.

[40] Y. LOU, P. YIN, Q. HE, AND J. XIN, *Computing sparse representation in a highly coherent dictionary based on difference of l_1 and l_2,* J. Sci. Comput., 64(1) (2015), pp. 178–196.

[41] P. D. TAO ET AL., *The dc (difference of convex functions) programming and dca revisited with dc models of real world nonconvex optimization problems,* Ann. Operations Res., 133(1-4) (2005), pp. 23–46.

[42] L. I. RUDIN, S. OSHER, AND E. FATEMI, *Nonlinear total variation based noise removal algorithms,* Phys. D Nonlinear Phenomena, 60(1-4) (1992), pp. 259–268.

[43] R. CHOKSI, Y. VAN GENNIP, AND A. OBERMAN, *Anisotropic total variation regularized l^1-approximation and denoising/deblurring of 2D bar codes,* (2010), arXiv:1007.1035.

[44] A. FISCHER, *A special newton-type optimization method,* Optimization, 24(3-4) (1992), pp. 269–284.

[45] R. B. POTTS, *Some generalized order-disorder transformations,* in: Mathematical Proceedings of the Cambridge Philosophical Society, Cambridge University Press, 48 (1952), pp. 106–109.

[46] D. MUMFORD, AND J. SHAH, *Boundary detection by minimizing functionals,* in: IEEE Confer-

ence on Computer Vision and Pattern Recognition, San Francisco, 17 (1985), pp. 137–154.
[47] E. J. CANDES, J. K. ROMBERG, AND T. TAO, *Stable signal recovery from incomplete and inaccurate measurements,* Communications on Pure and Applied Mathematics: A Journal Issued by the Courant Institute of Mathematical Sciences, 59(8) (2006), pp. 1207–1223.
[48] E. J. CANDES, AND T. TAO, *Decoding by linear programming,* IEEE Transactions on Information Theory, 51(12) (2005), pp. 4203–4215.
[49] Z. XU, X. CHANG, F. XU, AND H. ZHANG, *$L_{1/2}$ regularization: A thresholding representation theory and a fast solver,* IEEE Transactions on Neural Networks and Learning Systems, 23(7) (2012), pp. 1013–1027.
[50] S. ZHANG, AND J. XIN, *Minimization of transformed L_1 penalty: closed form representation and iterative thresholding algorithms,* (2014), arXiv preprint arXiv:1412.5240.
[51] T. ZHANG, *Multi-stage convex relaxation for learning with sparse regularization,* Adv. Neural Information Processing Systems, (2009), pp. 1929–1936.
[52] P. YIN, Y. LOU, Q. HE, AND J. XIN, *Minimization of ℓ_{1-2} for compressed sensing,* SIAM J. Sci. Comput., 37(1) (2015), pp. A536–A563.
[53] Y. WANG, J. YANG, W. YIN, AND Y. ZHANG, *A new alternating minimization algorithm for total variation image reconstruction,* SIAM J. Imag. Sci., 1(3) (2008), pp. 248–272.
[54] C. WU, AND X.-C. TAI, *Augmented lagrangian method, dual methods, and split bregman iteration for rof, vectorial tv, and high order models,* SIAM J. Imag. Sci., 3(3) (2010), pp. 300–339.
[55] M. A. FIGUEIREDO, AND J. M. BIOUCAS-DIAS, *Restoration of poissonian images using alternating direction optimization,* IEEE Trans. Image Process., 19(12) (2010), pp. 3133–3145.
[56] X. GUO, Y. LI AND T. ZENG, *A finite difference scheme for caputo-fabrizio fractional differential equations,* Int. J. Numer. Anal. Model., 17(2) (2020), pp. 195–211.
[57] K. ALSABTI, S. RANKA, AND V. SINGH, *An efficient k-means clustering algorithm,* 1997.
[58] J. A. HARTIGAN, AND M. A. WONG, *Algorithm as 136: A k-means clustering algorithm,* J. Royal Statistical Society Series C, (Applied Statistics) 28(1) (1979), pp. 100–108.
[59] A. LIKAS, N. VLASSIS, AND J. J. VERBEEK, *The global k-means clustering algorithm,* Pattern Recognition, 36(2) (2003), pp. 451—461.
[60] T. KANUNGO, D. M. MOUNT, N. S. NETANYAHU, C. D. PIATKO, R. SILVERMAN, AND A. Y. WU, *An efficient k-means clustering algorithm: Analysis and implementation,* IEEE Trans. Pattern Anal. Machine Intelligence, 7 (2002), pp. 881–892.
[61] J. C. BEZDEK, R. EHRLICH, AND W. FULL, *Fcm: The fuzzy c-means clustering algorithm,* Comput. Geosci., 10(2-3) (1984), pp. 191–203.
[62] W. WANG, Y. ZHANG, Y. LI, AND X. ZHANG, *The global fuzzy c-means clustering algorithm,* in: 2006 6th World Congress on Intelligent Control and Automation, IEEE, 1 (2006), pp. 3604–3607.
[63] F. LI, AND J. QIN, *Robust fuzzy local information and l_p-norm distance-based image segmentation method,* IET Imag. Process., 11(4) (2017), pp. 217–226.
[64] ANTONIN CHAMBOLLE, *An algorithm for total variation minimization and applications,* J. Math. Imag. Vision, 20(1-2) (2004), pp. 89–97.
[65] JEAN-BAPTISTE HIRIART-URRUTY AND CLAUDE LEMARECHAL, *Convex analysis and minimization algorithms I: fundamentals,* Springer Sci. Business Media, (2013), 305.
[66] F. LI, M. K. NG, T. Y. ZENG, AND C. SHEN, *A multiphase image segmentation method based on fuzzy region competition,* SIAM J. Imag. Sci., 3(3) (2010), pp. 277–299.
[67] J. LIU, X.-C. TAI, S. LEUNG, AND H. HUANG, *A new continuous max-flow algorithm for multiphase image segmentation using super-level set functions,* J. Visual Commun. Imag. Representation, 25(6) (2014), pp. 1472–1488.

[68] D. WANG, H. LI, X. WEI, AND X.-P. WANG, *An efficient iterative thresholding method for image segmentation,* J. Comput. Phys., 350 (2017), pp. 657—667.
[69] X. CAI, R. CHAN, C.-B. SCHONLIEB, G. STEIDL, AND T. ZENG, *Linkage between piecewise constant mumford-shah model and rudin-osher-fatemi model and its virtue in image segmentation,* SIAM J. Sci. Comput., 41(6) (2019), pp. B1310–B1340.
[70] P. DAMAYANTI, D. YUNIASRI, R. SARNO, A. FAJAR, AND D. RAHMAWATI, *Corpus callosum segmentation from brain MRI images based on level set method,* 2020 International Seminar on Application for Technology of Information and Communication, (iSemantic) (2020), pp. 155–160.
[71] G. GU, S. JIANG, AND J. YANG, *A tvscad approach for image deblurring with impulsive noise,* Inverse Problems, 33(12) (2017), 125008.
[72] T. WU, AND J. SHAO, *Non-convex and convex coupling image segmentation via TGpV regularization and thresholding,* Adv. Appl. Math. Mech., 12 (2020), pp. 849–878.
[73] F. FANG, F. LI, AND T. ZENG, *Reducing spatially varying out-of-focus blur from natural image,* Inverse Problems Imag., 11 (1) (2017), 65.
[74] M. K. NG, X. YUAN, AND W. ZHANG, *Coupled variational image decomposition and restoration model for blurred cartoon-plus-texture images with missing pixels,* IEEE Trans. Image Process., 22(6) (2013), pp. 2233–2246.
[75] Z. JIA, M. K. NG, AND G.-J. SONG, *Robust quaternion matrix completion with applications to image inpainting,* Numer. Linear Algebra Appl., 26(4) (2019), e2245.
[76] S. NOWOZIN, *Optimal decisions from probabilistic models: the intersection-over-union case,* in: Proceedings of the IEEE Conference on Computer Vision and Pattern Recognition, (2014), pp. 548–555.
[77] M. EVERINGHAM, S. A. ESLAMI, L. VAN GOOL, C. K. WILLIAMS, J. WINN, AND A. ZISSERMAN, *The pascal visual object classes challenge: A retrospective,* Int. J. Comput. Vision, 111(1) (2015), pp. 98–136.